Effects of swirl intensity on interfacial and wall friction factors of annular flows in a vertical pipe

Koto, Ryoya
Kurimoto, Ryo
Imaizumi, Atsuya
Hayashi, Kosuke
Tomiyama, Akio

(Citation)
Nuclear Engineering and Design,399:112001

(Issue Date)
2022-12-01

(Resource Type)
journal article

(Version)
Accepted Manuscript

(URL)
https://hdl.handle.net/20.500.14094/0100477356

Effects of swirl intensity on interfacial and wall friction factors of annular flows in a vertical pipe

Ryoya Koto, Ryo Kurimoto*, Atsuya Imaizumi, Kosuke Hayashi, Akio Tomiyama

Graduate School of Engineering, Kobe University

1-1, Rokkodai, Nada, Kobe, Japan.

*Corresponding author: kurimoto@mech.kobe-u.ac.jp

Highlights

- Effects of swirl intensity on interfacial and wall friction factors were investigated.
- Applicability of two-fluid and three-fluid models was discussed.
- Interfacial and wall friction factor correlations with the interfacial swirl number were developed.

Abstract

Interfacial and wall friction factors, f_i and f_w, of air-water swirling annular flows in a vertical pipe of diameter D = 30 mm were measured in three sections of L^* (= L/D) = 7.3, 13 and 31, where L is the distance from a swirler. The gas and liquid volumetric fluxes, J_G and J_L, were $12.5 \leq J_G \leq 20.0$ m/s and $0.070 \leq J_L \leq 0.213$ m/s, respectively. The interfacial swirl number, s_i, defined by $V_{i\theta}/V_{iz}$, where $V_{i\theta}$ and V_{iz} are the azimuthal and axial components of interfacial velocity, was introduced as an indicator of swirl intensity. For z^* (= z/D) ≤ 7, where z is the axial coordinate in the test section, the s_i increased with z^* at low

J_G and J_L, and slightly decreased with z^* at high J_G and J_L. The s_i decreased for $z^* > 7$ and reached zero at $z^* \approx 30$. The f_w estimated using the three-fluid model was larger than that estimated using the two-fluid model since the droplet flow rate was not negligible even in swirling annular flows. The three-fluid model was therefore more appropriate for evaluation of f_i and f_w than the two-fluid model. The ratio f_w^* increased with $\bar{s}_i$ for $\bar{s}_i > 0.25$, where f_w^* is the ratio of f_w to that of non-swirling flows and $\bar{s}_i$ is the averaged value of s_i in the section. The ratio f_i^* increased with $\bar{s}_i$ for $\bar{s}_i > 0.18$, where f_i^* is the ratio of f_i to that of non-swirling flows. Correlations in terms of $\bar{s}_i$ have prospect to evaluate the f_i and f_w in swirling annular flows.

Keywords: Swirling annular flow; Interfacial friction factor; Wall friction factor; Two-fluid model; Three-fluid model

1. Introduction

The steam separator of a boiling water reactor (BWR) separates steam-water two-phase flows generated in the reactor core into water and steam. A swirling annular flow is formed in the separator by the centrifugal force caused by stationary vanes of a swirler. The steam separator is expected not to cause large pressure drops, which may induce the onset of density-wave oscillation in the boiling system. It is therefore important to accurately predict the pressure drop of swirling annular flows when designing steam separators.

Most of numerical codes for thermal-hydraulic analyses adopt a one-dimensional two-fluid model or a multi-fluid model. There models require closure relations for the interfacial and wall friction factors, f_i and f_w. Several correlations of f_i and f_w for non-swirling annular flows have been proposed, e.g. Wallis (1969), Hewitt and Hall-Taylor (1970) and Fukano

and Furukawa (1998). Kataoka et al. (2009) showed that the one-dimensional two-fluid model gives reasonable predictions of pressure drops in air-water swirling annular flows by multiplying a factor of five to the Wallis model. Funahashi et al. (2018) obtained experimental data of f_i and f_w in air-water swirling annular flows in a vertical pipe. Their f_i and f_w were larger than those evaluated with the Wallis model. The swirl motion increases f_i and f_w, and therefore the effects of the swirl motion should be accounted for in modelling f_i and f_w for accurate predictions of the pressure drop in the steam separator. There are, however, no experimental data on the relation between the swirl intensity and the friction factors.

Funahashi et al. (2018) utilized the two-fluid model for the evaluation of f_i and f_w in the swirling annular flows since most of droplets in a swirling annular flow deposit onto the liquid film (Kataoka et al. 2008). The three-fluid model, however, should be used for evaluating f_i and f_w if the volumetric flux, J_E, of droplets has non-negligible influence. Measurements of J_E are required to make this point clear.

We therefore measured the pressure drop and void fraction of air-water swirling annular flows in three sections in the vertical direction to investigate the relation between the swirl intensity and the friction factors. Flow images were recorded using a high-speed video camera to measure velocities of interfacial waves, which were utilized to obtain the interfacial swirl number representing the swirl intensity. The f_i and f_w were evaluated based on the one-dimensional two-fluid model. After validating f_i and f_w based on the two-fluid model, we also evaluated f_i and f_w based on the one-dimensional three-fluid model as well. Correlations of f_i and f_w expressed in terms of the interfacial swirl number were also developed.

2. Experimental method

2.1 Experiment setup

Fig. 1 shows the experimental setup, which consists of the test section, the swirler, the entrance section, the air-water mixing section, the upper tank, the water tank, the bypass section, the water supply system and the air supply system. The inner diameters, D, of the test section and the entrance section were 30 mm. The lengths of the test section and the entrance section were 1170 and 305 mm, respectively. The test section was made of transparent acrylic resin for flow observation. Air was supplied from the compressor (ANEST IWATA, SLP110) to the mixing section through the flowmeter (NIPPON FLOW CELL, FLT-N) and the regulator (CKD, R6000-20). The pump (Iwaki, MD-40R-N) supplied tap water stored in the water tank to the mixing section through the flow meter (NIPPON FLOW CELL, FLT-N). An air-water two-phase flow flowed up in the entrance section and the swirler formed a swirling two-phase flow in the test section. After reaching the upper tank, air was discharged into atmosphere and water returned to the water tank. The temperatures of air and water were 298 ± 2 K. The experiments were carried out at atmospheric pressure.

The swirler shown in Fig. 2 was installed between the entrance section and the test section, i.e. 305 mm above the mixing section. The axial coordinate z in the test section is 0 at the top end of the swirler. The swirler made of ABS (Acrylonitrile Butadiene Styrene) resin had the hub of 6 mm diameter and eight stationary vanes with the vane angle of 30° near the hub and of 60° at its perimeter.

The liquid-separation performance in the steam-water separator of an actual BWR can be reproduced in a downscaled air-water separator by setting the quality and the two-phase centrifugal force per unit volume of the two separators the same (Katono et al., 2014). Based

on this scaling law, the nominal operating condition of the advanced BWR corresponds to J_G = 18.7 m/s and J_L = 0.129 m/s in the present system. The ranges of the gas and liquid volumetric fluxes were determined in such a way as to include these volumetric fluxes, i.e. $12.5 \leq J_G \leq 20.0$ m/s and $0.070 < J_L < 0.22$ m/s.

2.2 Measurement method and flow observation

The pressure drop, ΔP, and void fraction, α_G, were measured in three sections of L^* (= L/D) = 7.3, 13, 31, where L is the distance from the swirler to the center of each measurement section. The L^* = 7.3 corresponds to the distance from the swirler to the third pick-off ring in an actual BWR separator (Nakao et al., 1998). The pressure drop was measured using differential pressure transducers (VALIDYNE ENGINEERING, DP45) and the pressure taps were at $z = L \pm 145$ mm. The sampling frequency was 1000 Hz and the sample number was 60000. The uncertainty estimated at 95% confidence in the time-averaged pressure drop was less than 1.1%.

The ΔP consists of the frictional pressure drop ΔP_F and the static pressure drop ΔP_G:

$$\Delta P = \Delta P_F + \Delta P_G \tag{1}$$

since the acceleration pressure drop is negligible. The latter is given by

$$\Delta P_G = [\alpha_G \rho_G + (1 - \alpha_G)\rho_L]gh \tag{2}$$

where α is the volume fraction, ρ the density, g the acceleration of gravity, h the distance between the pressure taps, and the subscripts G and L denote the gas and liquid phases,

respectively. ΔP_F is calculated by substituting the measured values of ΔP and α_G into the following equation:

$$\Delta P_F = \Delta P - [\alpha_G \rho_G + (1 - \alpha_G)\rho_L]gh \tag{3}$$

The void fraction was measured in each measurement section by using quick-closing valves (QCVs) (Funahashi et al., 2018). Two QCVs were installed at $z = L \pm 190$ mm. Another QCV was installed in the bypass connecting the entrance section and the water tank and was opened when two QCVs were closed to prevent a large pressure surge in the pipe. The instantaneous void fraction of the ith measurement, α_{Gi}, was obtained by measuring the height, H_i, of liquid accumulated in the measurement section:

$$\alpha_{Gi} = 1 - H_i/H \tag{4}$$

where H is the distance between the two QCVs. The ensemble-averaged void fraction was given by

$$\alpha_G = \frac{1}{n}\sum_{i=1}^{n} \alpha_{Gi} \tag{5}$$

where n is the total number of measurements, which was adjusted so as to obtain an accurate α_G, and ranged from 30 to 100. The uncertainty estimated at 95% confidence in α_G was less than 0.65%.

Flows in the pipe were observed using a high-speed video camera (IDT, Motion Pro X-3). The frame rate and exposure time were 2500 frames/s and 400 μs, respectively. The

particle image velocimetry (PIV) was applied to images to measure the azimuthal and axial components, $V_{i\theta}$ and V_{iz}, of interfacial wave velocity at the gas-liquid interface. Optical distortion due to the curved surface of the pipe was corrected based on the Snell's law. Interrogation areas of 9 x 9 mm (60 x 60 pixels) were located at the center of the pipe. 10000 sequential images were used for the calculation of $V_{i\theta}$ and V_{iz} in each condition. The uncertainties estimated at 95% confidence in $V_{i\theta}$ and V_{iz} at $L^* = 7.3$ were less than 2.8% and 1.7%, respectively.

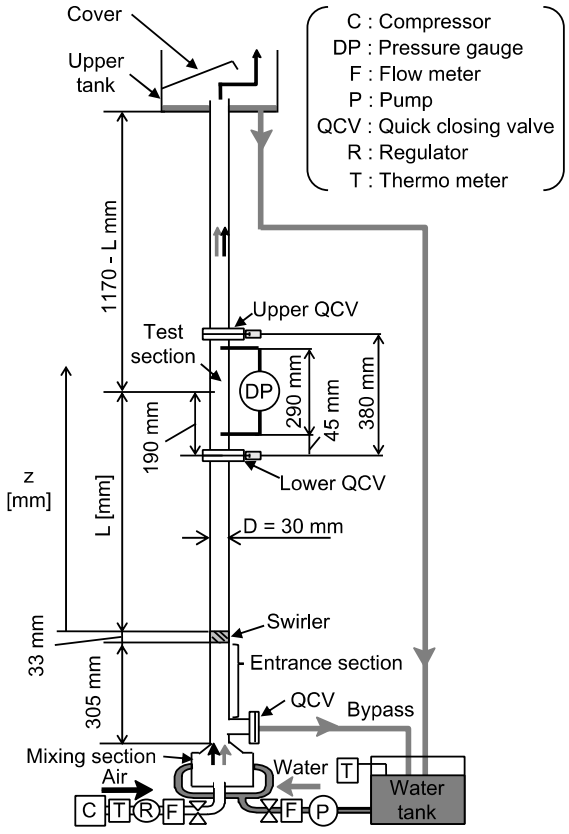

Fig. 1 Experimental setup

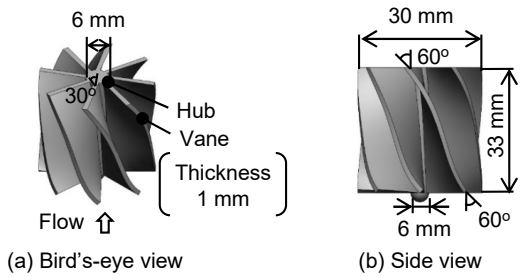

Fig. 2 Swirler

2.3 Evaluation of f_i and f_w based on two-fluid model

The one-dimensional two-fluid model for a fully-developed annular flow in a vertical pipe assumes that an annular liquid film flows along the pipe wall and the gas phase flows in the center region of the pipe. The volume fractions satisfy

$$\alpha_G + \alpha_L = 1 \tag{6}$$

The momentum conservation equations of the gas and liquid phases are given by

$$\alpha_G \frac{\partial P}{\partial z} = -\alpha_G \rho_G g - \frac{4\tau_i \sqrt{\alpha_G}}{D} \tag{7}$$

$$\alpha_L \frac{\partial P}{\partial z} = -\alpha_L \rho_L g + \frac{4\left(\tau_i \sqrt{\alpha_G} - \tau_w\right)}{D} \tag{8}$$

where P is the pressure, τ the shear stress and the subscripts i and w denote the interface and the wall, respectively. The τ_i and τ_w are expressed in terms of f_i and f_w, respectively, as follows:

$$\tau_i = f_i \frac{\rho_G (V_G - V_L)^2}{2} \tag{9}$$

$$\tau_w = f_w \frac{\rho_L V_L^2}{2} \tag{10}$$

where V is the phase-averaged velocity given by $V = J/\alpha$. Solving Eqs. (7) and (8) for f_i and f_w yields

$$f_i = \frac{-D\alpha_G}{2\rho_G \sqrt{\alpha_G}(V_G - V_L)^2}\left(\frac{\partial P}{\partial z} + \rho_G g\right) \tag{11}$$

$$f_w = \frac{-D}{2\rho_L V_L^2}\left[\frac{\partial P}{\partial z} + \alpha_G \rho_G g + (1 - \alpha_G)\rho_L g\right] \tag{12}$$

Experimental data of α_G and $\partial P/\partial z$ are required for the evaluation of f_i and f_w using Eqs. (11) and (12).

2.4 Evaluation of f_i and f_w based on three-fluid model

The one-dimensional three-fluid model for a fully-developed annular flow in a vertical pipe accounts for the presence of droplets entrained in the gas-core. The volume fractions satisfy

$$\alpha_G + \alpha_L = \alpha_G + \alpha_F + \alpha_E = 1 \tag{13}$$

where the subscripts F and E denote the liquid film and the droplets, respectively. The momentum conservation equations of the gas phase, the liquid film and the droplets are

given by

$$\alpha_G \frac{\partial P}{\partial z} = -\alpha_G \rho_G g - \frac{4\tau_i \sqrt{\alpha_G}}{D} - \gamma_{EG}\tau_{EG} \tag{14}$$

$$\alpha_F \frac{\partial P}{\partial z} = -\alpha_F \rho_L g + \frac{4\left(\tau_i \sqrt{\alpha_G} - \tau_w\right)}{D} \tag{15}$$

$$\alpha_E \frac{\partial P}{\partial z} = -\alpha_E \rho_L g + \gamma_{EG}\tau_{EG} \tag{16}$$

where γ_{EG} is the interfacial area concentration of droplets, and τ_{EG} the shear stress acting on the droplet interfaces. The shear stresses τ_i and τ_w are given by

$$\tau_i = f_i \frac{\rho_G (V_G - V_F)^2}{2} \tag{17}$$

$$\tau_w = f_w \frac{\rho_L V_F^2}{2} \tag{18}$$

Solving Eqs. (14)-(16) for f_i and f_w yields

$$f_i = \frac{-D(\alpha_G + \alpha_E)}{2\rho_G \sqrt{\alpha_G}(V_G - V_F)^2}\left(\frac{\partial P}{\partial z} + \rho_M g\right) \tag{19}$$

$$f_w = \frac{-D}{2\rho_L V_F^2}\left[\frac{\partial P}{\partial z} + \alpha_G \rho_G g + (1 - \alpha_G)\rho_L g\right] \tag{20}$$

where ρ_M is the mixture density defined by

$$\rho_M = \frac{\alpha_G \rho_G + \alpha_E \rho_L}{\alpha_G + \alpha_E} \tag{21}$$

In addition to α_G and $\partial P/\partial z$, data of α_E and V_F are required for the evaluation of f_i and f_w.

3. Results and discussion

3.1 Swirl intensity

Fig. 3 shows the axial distributions of $V_{i\theta}$ and V_{iz}, which take the largest values at the outlet of the swirler and increase with increasing J_G and J_L. For z^* (= z/D) $\leq$ 7, $V_{i\theta}$ and V_{iz} decrease with increasing z^*, while V_{iz} becomes almost constant for $z^* > 7$. On the other hand, $V_{i\theta}$ keeps decreasing until reaching zero at $z^* \approx 30$.

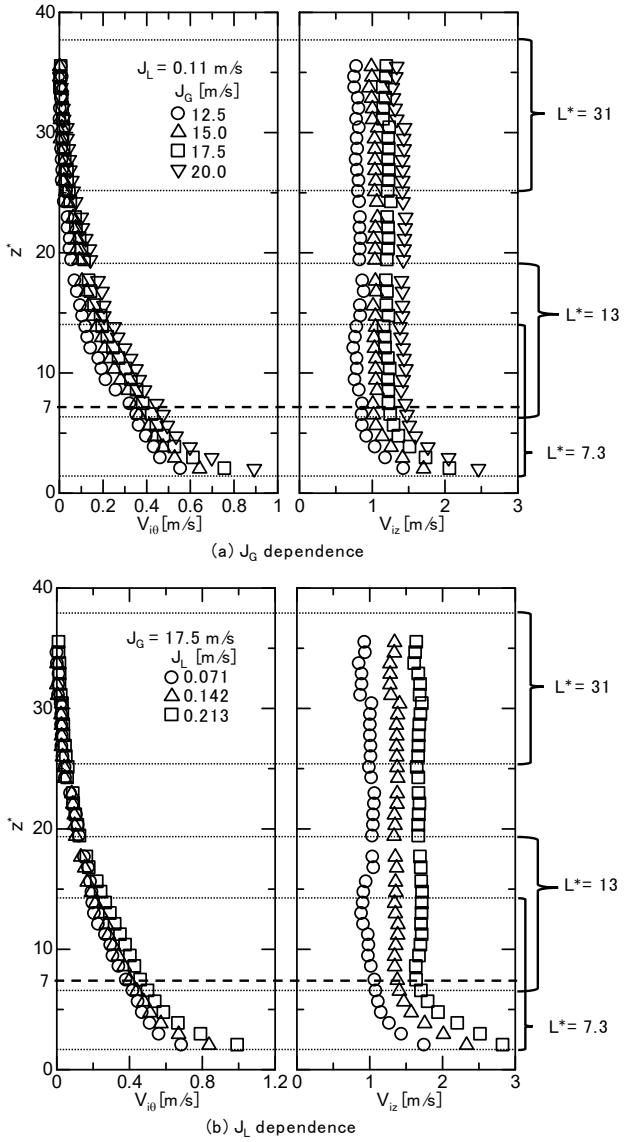

Fig. 3 Axial distributions of $V_{i\theta}$ and V_{iz}

The following swirl number, s, has been used for the evaluation of swirl intensity of a single-phase flow (Hatazawa, 1998):

$$s = \frac{\int_0^{D/2}\int_0^{2\pi} \rho V_\theta V_z r^2 d\theta\, dr}{\frac{D}{2}\int_0^{D/2}\int_0^{2\pi} \rho V_z^2 r d\theta\, dr} \tag{22}$$

where r is the radial coordinate. The swirl number requires the data of V_θ and V_z for the entire range of r and θ in the integration. The simplified swirl number, s_s, defined by using V_θ/V_z at $2r/D = 0.95$ instead of the integration has often been used (Yajnik and Subbaiah 1973; Hatazawa 1998; Hatazawa 2011) since the characteristics of swirling flows strongly appear in the vicinity of a pipe wall. Based on the concept of s_s, we introduce the following interfacial swirl number, s_i, as an indicator of swirl intensity of two-phase annular flow:

$$s_i = \frac{V_{i\theta}}{V_{iz}} \tag{23}$$

Fig. 4 shows the axial distributions of s_i. For $z^* \leq 7$, s_i increases with z^* at low J_G and J_L, whereas s_i slightly decreases with z^* at high J_G and J_L. The increase in s_i with respect to z^* after passing through the swirler is caused by the weak decay rate of $V_{i\theta}$. An increase in s_s after passing through a swirl was also observed in a single-phase swirling flow (Yajnik and Subbaiah 1973; Hatazawa 1998). For $z^* > 7$, s_i decreases with increasing z^* and the dependence of s_i on J_G is small in the present condition. This result indicates that flows at $L^* = 7.3$ are in a swirling flow regime and those at $L^* = 31$ are in a non-swirling flow regime.

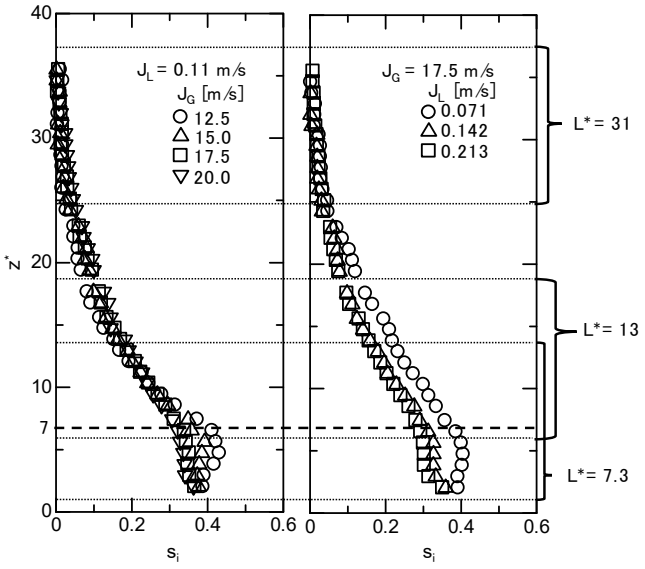

Fig. 4 Axial distributions of s_i

3.2 Void fraction and pressure drop

Figs. 5(a)-(c) show measured α_G at $L^* = 7.3$, 13 and 31, respectively. The α_G increases with increasing J_G and decreasing J_L. Fig. 5(d) shows the α_G data at $J_L = 0.071$, 0.142 and 0.213 m/s to make the L^* dependence clear. The difference in α_G between the sections is less than 1.2%, and therefore, the effect of s_i on α_G is weak.

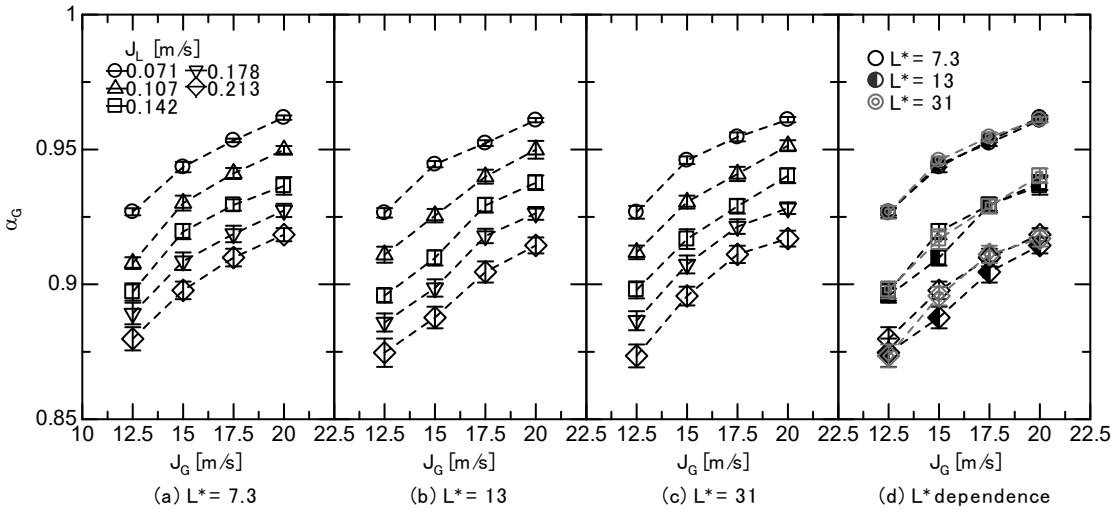

Fig. 5 Void fraction α_G

Fig. 6 shows effects of J_G, J_L and L^* on ΔP. The ΔP increases with increasing J_G and J_L and decreases with increasing L^*, which means that ΔP decreases with increasing the swirl intensity as reported in Liu et al. (2020). Figs. 7 (a) and (b) show ΔP_G and ΔP_F, respectively. The static pressured drop ΔP_G is independent of L^*, since α_G is not affected by L^* as shown in Fig. 5(d). In contrast, the frictional pressure drop ΔP_F decreases with increasing L^*, in other words, with increasing the swirl intensity.

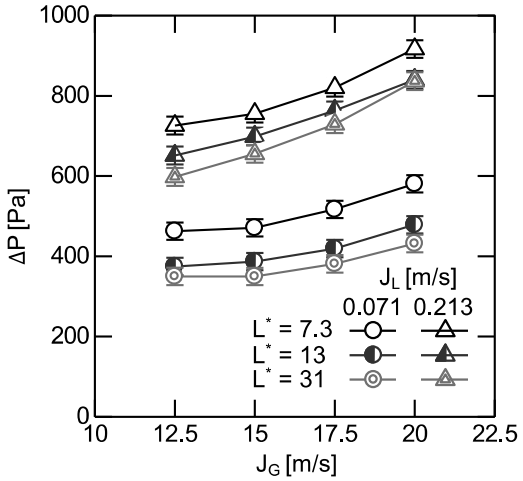

Fig. 6 Pressure drop ΔP

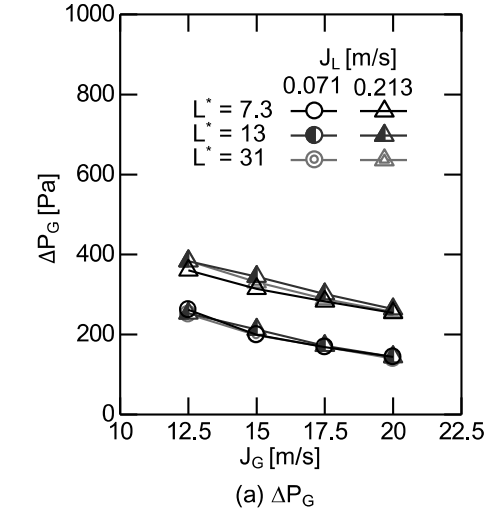

Fig. 7 ΔP_G and ΔP_F

3.3 f_i and f_w based on two-fluid model

Fig. 8 shows the relation between f_i and α_L. The f_i increases with increasing α_L and decreasing L^*, i.e. f_i increases with increasing the swirl intensity. The solid and broken lines are drawn by using the two representative f_i correlations for non-swirling annular flows, Eq. (24) (Wallis, 1969) and Eq. (25) (Fukano and Furukawa, 1998):

$$f_i = 0.005(1 + 75\alpha_L) \tag{24}$$

$$f_i = \frac{0.425(1+3\alpha_L)^8}{\left(12+\frac{\nu_L}{\nu_W}\right)^{1.33}} \tag{25}$$

where ν is the kinematic viscosity and the subscript *W* denotes water. The former correlation is for a fully-developed annular flow, whereas the latter is for a developing annular flow. The f_i data at L^* = 31, i.e. non-swirling flow, agree well with the Fukano-Furukawa correlation for $\alpha_L \leq 0.1$, although the increasing rate $df_i/d\alpha_L$ of the correlation is somewhat different from the data. The data at L^* = 13 and 31 for $\alpha_L > 0.1$ are lower than the correlation. The main cause of this difference between Eq. (25) and the data for $\alpha_L > 0.1$ is the flow pattern difference. The video image analyses confirmed that the flow pattern at L^* = 13 and 31 for $\alpha_L > 0.1$ is not annular but the transition regime between churn and annular flows. Weak interfacial shear stress due to weak upward gas velocity (low J_G) may retard the liquid velocity in the upward direction (Kurimoto et al., 2022), causing the flow pattern transition to churn flow and decrease in the form drag.

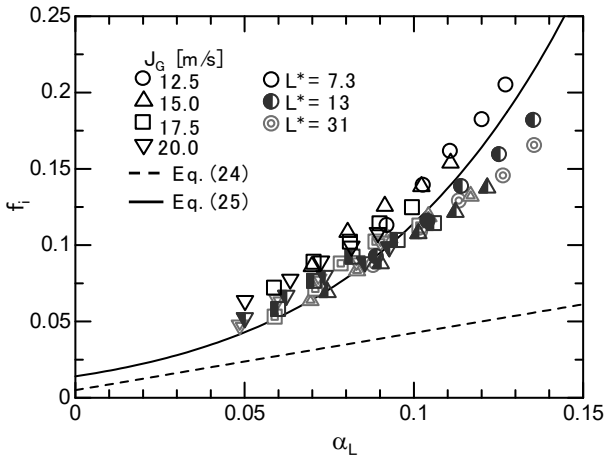

Fig. 8 f_i based on two-fluid model

The relation between f_w and the liquid Reynolds number, Re_L, is shown in Fig. 9, where Re_L is defined by

$$Re_L = \frac{J_L D}{\nu_L} \tag{26}$$

The solid lines in the figure represent the following correlation of f_w for non-swirling annular flows (Wallis, 1969; Hewitt and Hall-Taylor, 1970):

$$f_w = \begin{cases} 16/Re_L & \text{for } Re_L \leq 2300 \\ 0.079/Re_L^{0.25} & \text{for } Re_L > 2300 \end{cases} \tag{27}$$

The f_w data for L^* = 7.7 are larger than Eq. (27) and those for L^* =13 and 31 are smaller than Eq. (27). The latter implies that the actual volumetric flux of the liquid film were smaller than J_L, i.e. some of the liquid phase might flow as droplets in the gas-core. The volume fraction of droplets might increase with increasing z^* due to the decrease in swirl intensity. We therefore evaluate f_i and f_w based on the three-fluid model in the next section.

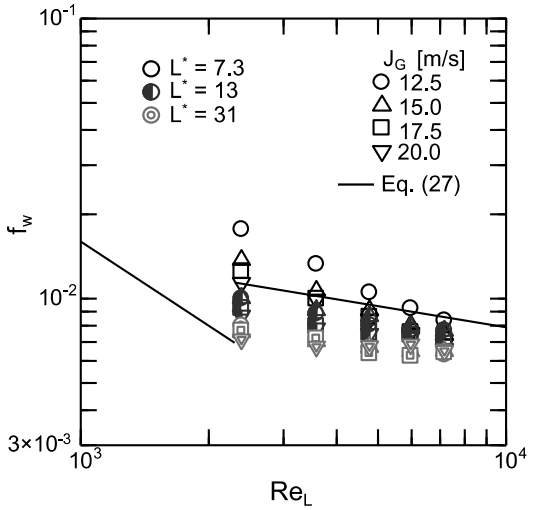

Fig. 9 f_w based on two-fluid model

3.4 f_i and f_w based on three-fluid model

As noted in section 2.4, α_E and V_F data are required to evaluate f_i and f_w based on the three-fluid model. The volume flow rate of the liquid film was measured using a pick-off-ring (POR) installed at $L^* = 7.3$, 13 or 31 (Fig. 10) to obtain the volumetric fluxes of droplets and the liquid film, J_E and J_F (= $J_L - J_E$). The tip of the POR was tapered off to smoothly collect the liquid film. Before installing the POR, the liquid film thicknesses were measured using a laser focus displacement meter (LFD) (KEYENCE, LR-9030) (Takamasa and Hazuku, 1998; Funahashi et al., 2016) to determine the gap thickness between the wall and the POR. An example of the measured instantaneous liquid film thicknesses is shown in Appendix A. The maximum liquid film δ_{99} defined as the value at 99% of the cumulative frequency distribution of the instantaneous liquid film thickness was less than 2.0 mm even at J_G = 12.5 m/s and J_L = 0.213 m/s, at which the mean liquid film is the thickest in all the experimental conditions. Furthermore, we measured the volume flow rate of the liquid film using two PORs with different gap thicknesses of 2.0 and 2.3 mm, and confirmed that both gave the same values of J_E. Hence the wall thickness of the POR and the gap thickness were

determined to be 0.5 and 2 mm, respectively.

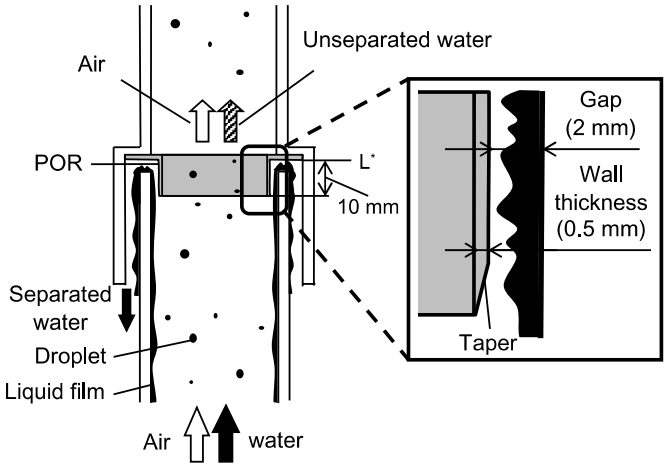

Fig. 10 Separation of liquid film using POR

Fig. 11 shows the relation between J_E and J_L. The solid and broken lines are the following correlations of the entrained liquid fraction E (= J_E/J_L) proposed by Oliemans et al. (1986) and Cioncolini and Thome (2010), respectively:

$$\frac{E}{1-E} = 10^{c_0}\rho_L^{c_1}\rho_G^{c_2}\mu_L^{c_3}\mu_G^{c_4}\sigma^{c_5}D^{c_6}J_L^{c_7}J_G^{c_8}g^{c_9} \tag{28}$$

$$E = (1 + 13.18We_C^{-0.655})^{-10.77} \tag{29}$$

where c_j (j = 0-9) are constants, μ the viscosity, σ the surface tension, and We_C the Weber number of the gas core defined by $We_C = \rho_C V_C^2 D_C/\sigma$. Here ρ_C is the droplets-laden gas-core density, V_C the core flow velocity and D_C the core flow hydraulic diameter. Both the measured and calculated J_E increase with increasing J_L. The measured J_E also increases with increasing L^*, i.e. with decreasing the swirl intensity. The measured J_E for J_G = 12.5

and 15.0 m/s, i.e. for weak centrifugal force cases, agree well with Eq. (28), whereas they approach Eq. (29) with increasing J_G. As expected, the droplet entrainment is enhanced due to the decay of swirling intensity. The J_E decreases with increasing J_G. This is because the increase in the centrifugal force due to the increase in J_G promotes the droplet deposition. The maximum and minimum E calculated using the measured J_E are 0.32 and 0.073, respectively.

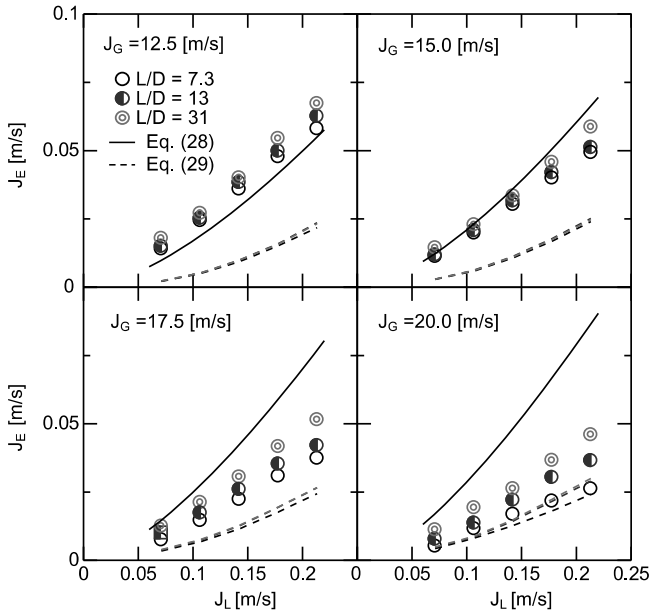

Fig. 11 Comparisons of J_E with correlations

The droplet fraction α_E and film velocity V_F can be calculated using the relations of $V = J/\alpha$ and $\alpha_L = \alpha_E + \alpha_F$ if the droplet velocity V_E is known. Although Azzopardi (1997) reported that the droplet velocity is about 80% of the gas velocity in non-swirling annular flows, there are no data of V_E in swirling annular flows. We therefore examined the sensitivity of V_E on evaluated f_i and f_w. If we assume that the drag coefficient is 0.4 and the droplet diameter is 500 μm, which might be too large for vertical annular flows (Fore and

Dukler, 1995; Zhang et al., 2019), V_E becomes about 70% of V_G. Since V_E is less than V_G due to the gravitational force in an upward flow, the upper bound of V_E/V_G is unity. We therefore calculated f_i and f_w at $V_E/V_G = 0.7$ and 1. The maximum values of the ratios, $f_i|_{0.7}/f_i|_1$ and $f_w|_{0.7}/f_w|_1$, where $f|_{0.7}/f|_1$ is the ratio of f at $V_E/V_G = 0.7$ to f at $V_E/V_G = 1$, in the present experimental range are 0.37% and 3.0%, respectively. The ratios are small, and therefore, V_E in the range of $0.7V_G$ to V_G does not affect f_i and f_w so much. We therefore assumed $V_E = 0.8V_G$.

Fig. 12 shows the relation between f_w based on the three-fluid model and the film Reynolds number, Re_F, defined by

$$Re_F = \frac{J_F D}{\nu_L} \tag{30}$$

The solid line is the f_w correlation, Eq. (27), calculated by using Re_F instead of Re_L. The f_w data are larger than those in Fig. 9. In addition, the lower bound of f_w at $L^* = 31$ (non-swirling flow) is close to Eq. (27). The f_w decreases with increasing J_G, which agrees with the observation by Funahashi et al. (2018). The f_w also decreases with increasing L^*, i.e. the decay of the swirl intensity causes the decrease in f_w. In a single-phase swirling flow with high swirl intensity, the axial velocity takes a wall-peaking distribution (Kitoh, 1991; Hatazawa, 1998). The large velocity gradient in the wall-peaking velocity distribution could be the cause of the increase in f_w.

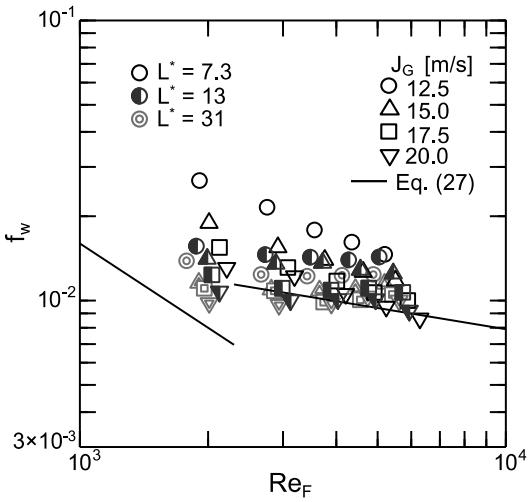

Fig. 12 f_w based on three-fluid model

Fig. 13 shows the relation between f_w^* and $\bar{s}_i$, where f_w^* is the ratio of f_w at $L^* = 7.3$ or 13 to f_w at $L^* = 31$, and the $\bar{s}_i$ is the mean value of s_i in the measurement section. The ratio is almost unity for $\bar{s}_i \leq 0.25$ and increases with $\bar{s}_i$ for $\bar{s}_i > 0.25$. As mentioned above, a single-phase swirling flow with high swirl intensity forms a wall-peaking distribution of the axial velocity, while that with low swirl intensity forms a core-peaking distribution (Kitoh, 1991; Hatazawa, 1998). Hatazawa (2011) reported that the transition from the core- to wall-peaking distributions takes place at $s_s \approx 0.27$ in single-phase flows. Thus, $\bar{s}_i = 0.25$ well corresponds to the transition from the core- to the wall-peaking distributions.

The f_w can be expressed as

$$f_w = f_w^*(\bar{s}_i) f_{w,ns} \tag{31}$$

where $f_{w,ns}$ is f_w for non-swirling flows, i.e. f_w at $L^* = 31$. The f_w^* is expressed in terms of $\bar{s}_i$:

$$f_w^*(\bar{s}_i) = \begin{cases} 7.2(\bar{s}_i - 0.25) + 1 & \text{for } \bar{s}_i > 0.25 \\ 1 & \text{for } \bar{s}_i \le 0.25 \end{cases} \tag{32}$$

The $f_{w,ns}$ is correlated as

$$f_{w,ns} = \frac{16}{Re_F^{7.2\times10^{-3}} Re_G^{0.67}} \tag{33}$$

where Re_G is the gas Reynolds number defined by

$$Re_G = \frac{J_G D}{\nu_G} \tag{34}$$

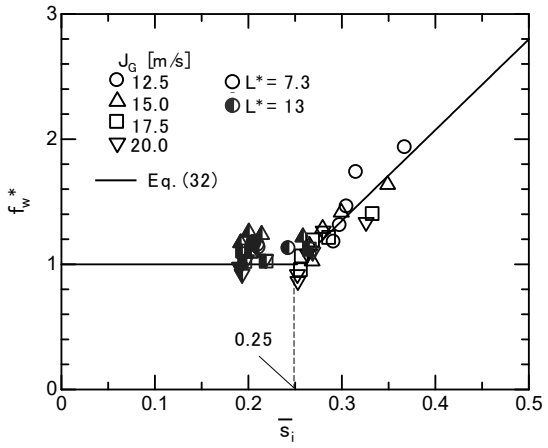

Fig. 13 Relation between f_w^* and $\bar{s}_i$

The comparison of f_w between the measured data and Eq. (31) is shown in Fig. 14. The correlation evaluates 93% of the measured data to within ±15% errors.

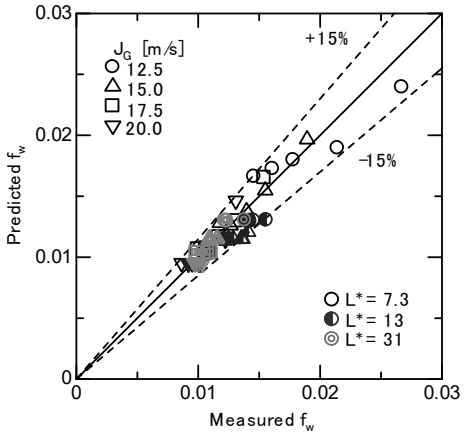

Fig. 14 Comparison between measured and predicted f_w

Fig. 15 shows the relation between f_i and α_F. The solid line is the f_i correlation, Eq. (25), calculated as $\alpha_L = \alpha_F$. Being similar to f_i based on the two-fluid model, f_i increases with increasing α_F and decreasing L^*. Difference between f_i of the two-fluid and three-fluid models is small. The largest difference is 9.4% at J_G = 12.5 m/s and J_L = 0.213 m/s at L^* = 31. There are two differences between Eqs. (11) and (19): the change from α_G to $\alpha_G + \alpha_E$ in the numerator; and the change from $V_G - V_L$ to $V_G - V_F$ in the denominator. The ratios of $\alpha_G + \alpha_E$ to α_G and $V_G - V_F$ to $V_G - V_L$ are 0.67 and 3.4 % at most, respectively. In contrast, the change from V_L^2 to V_F^2 in the denominators of Eqs. (12) and (20) results in the large change in f_w as shown in Figs. 9 and 12. The f_i data at L^* = 31 deviate from Eq. (25) for α_L > 0.1. 25% of the measured data are out of the range of $\pm$20% errors of Eq. (25).

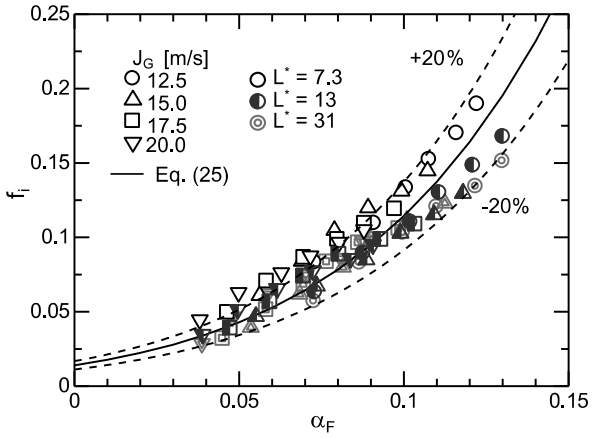

Fig. 15 f_i based on three-fluid model

Fig. 16 shows the relation between f_i^* and $\bar{s}_i$, where f_i^* is the ratio of f_i at L^* = 7.3 or 13 to f_i at L^* = 31. Being similar to f_w^*, the ratio f_i^* asymptotically approaches unity as $\bar{s}_i$ decreases to 0.18. This would be due to the increase in the form drag caused by swirl motion.

The interfacial friction factor f_i is expressed as

$$f_i = f_i^*(\bar{s}_i) f_{i,ns} \tag{35}$$

where $f_{i,ns}$ is f_i for non-swirling flows, i.e. f_i at L^* = 31. The ratio f_i^* is correlated with $\bar{s}_i$:

$$f_i^*(\bar{s}_i) = \begin{cases} 2.1(\bar{s}_i - 0.18) + 1 & \text{for } \bar{s}_i > 0.18 \\ 1 & \text{for } \bar{s}_i \leq 0.18 \end{cases} \tag{36}$$

The interfacial friction factor for non-swirling flows $f_{i,ns}$ is correlated in terms of f_G and α_F:

$$f_{i,ns} = f_G(1 + 120\alpha_F)^{1.2} \tag{37}$$

where f_G is given by

$$f_G = \frac{0.079}{Re_G^{0.25}} \tag{38}$$

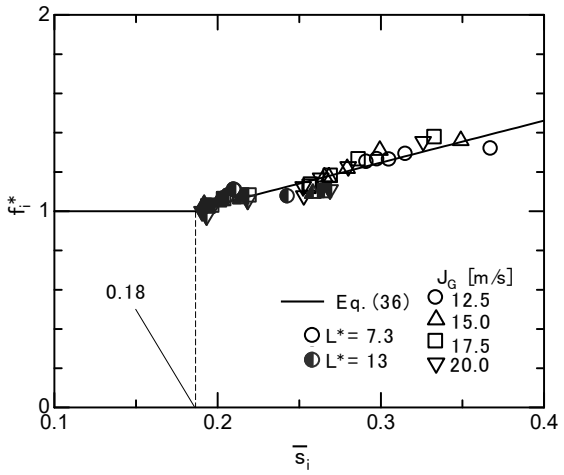

Fig. 16 Relation between f_i and $\bar{s}_i$

The comparison between the measured data and Eq. (35) is shown in Fig. 17. The correlation evaluates 90% of the measured data to within ±15% errors.

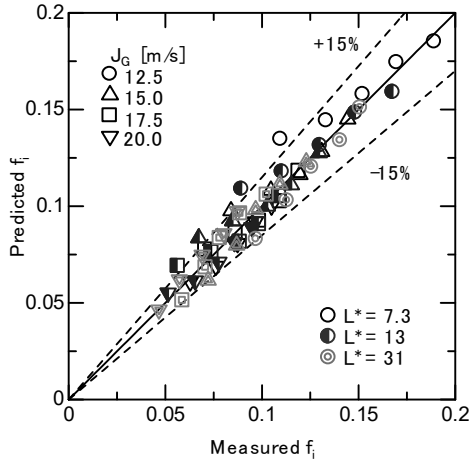

Fig. 17 Comparison between measured and predicted f_i

4. Conclusion

The interfacial and wall friction factors, f_i and f_w, of air-water swirling annular flows in a vertical pipe were investigated based on the steady-state one-dimensional two-fluid and three-fluid models. The pressure drops and void fractions of the swirling flows were measured in three sections of the pipe ($L^* = 7.3$, 13 and 31) to evaluate the effects of swirl intensity, and flows in the pipe were observed to obtain the azimuthal and axial components, $V_{i\theta}$ and V_{iz}, of interfacial velocity. The interfacial swirl number, s_i, was defined by $V_{i\theta}/V_{iz}$ to represent swirl intensity, and $\bar{s}_i$, which is the averaged value of s_i in each section, was introduced. For the evaluation of f_i and f_w based on the three-fluid model, the volume flow rate of the liquid film was measured using a pick-off ring. The following conclusions are obtained:

1. The three-fluid model is more appropriate for evaluation of f_i and f_w than the two-fluid model since entrained liquid fraction is not negligible even in swirling annular flows.
2. The ratio f_w^* of f_w to that of non-swirling flows is unity for $\bar{s}_i \leq 0.25$ and increases with $\bar{s}_i$ for $\bar{s}_i > 0.25$. This tendency implies that the transition of the axial velocity distribution from core-peaking to wall-peaking due to the increase in the swirl intensity causes the increase in f_w.
3. The ratio f_i^* of f_i to that of non-swirling flows asymptotically approaches unity as $\bar{s}_i$ decreases to 0.18. This means that the form drag increases with $\bar{s}_i$ for $\bar{s}_i > 0.18$.
4. Correlations in terms of $\bar{s}_i$ have prospect to evaluate the f_i and f_w in swirling annular flows.

The developed correlations of f_i and f_w expressed in terms of $\bar{s}_i$ evaluates the present experimental data to within $\pm$15% errors.

Acknowledgement

The authors would like to express their gratitude to Mr. Yoshihiro Yahara for his contribution to experiments and discussion.

Appendix A. Instantaneous liquid film thickness

Fig. A1 shows a time series of the instantaneous liquid film measured using a LFD at J_G = 12.5 m/s and J_L = 0.213 m/s, at which the mean liquid film is the thickest in all experimental conditions. The maximum liquid film thickness δ_{99} was less than 2.0 mm, where δ_{99} is defined as the value at 99% of the cumulative frequency distribution of the instantaneous liquid film.

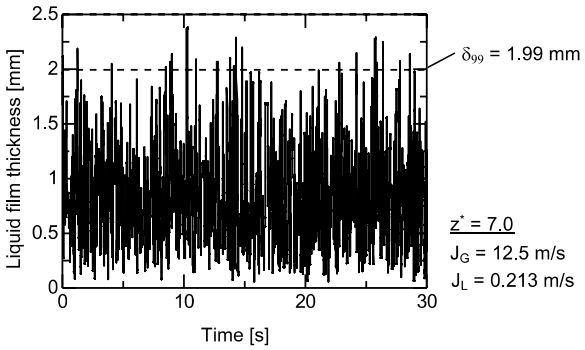

Fig. A1 Time series of instantaneous liquid film thickness

at J_G = 12.5 m/s and J_L = 0.213 m/s

Reference

Azzopardi, B. J., 1997. Drops in annular two-phase flow, International Journal of Multiphase Flow, Vol. 23, pp. 1-53.

Cioncolini, A., and Thome, J. R., 2010. Prediction of the entrained liquid fraction in vertical annular gas-liquid two-phase flow, International Journal of Multiphase Flow, Vol. 36, pp.

293-302.

Fore, L. B., and Dukler, A. E., 1995. The distribution of drop size and velocity in gas-liquid annular flow, International Journal of Multiphase Flow, Vol. 21, pp. 137-149.

Fukano, T., and Furukawa, T., 1998. Prediction of the effects of liquid viscosity on interfacial shear stress and frictional pressure drop in vertical upward gas-liquid annular flow, International Journal of Multiphase Flow, Vol. 24, No. 5, pp. 587-603.

Funahashi, H., Hayashi, K., Hosokawa, S., and Tomiyama, A., 2016. Study on two-phase swirling flows in a gas-liquid separator with three pick-off rings, Nuclear Engineering and Design, Vol. 308, pp. 205-213.

Funahashi, H., Vierow Kirkland, K., Hayashi, K., Hosokawa, S., and Tomiyama, A., 2018. Interfacial and wall friction factors of swirling annular flow in a vertical pipe, Nuclear Engineering and Design, Vol. 330, pp. 97-105.

Hatazawa, M., 1998. Characteristics of turbulent swirling flow in a straight pipe -Swirl effect on pressure loss-, Journal of Japanese Society of Fluid Mechanics, Vol. 17, pp. 202-213 (in Japanese).

Hatazawa, M., 2011. Characteristics of turbulent swirling flow in a straight pipe -Change in axial velocity with swirl decay-, Proc. of Chugoku-Shikoku Shibu Dai48ki Soukai-Kouenkai, the Japan Society of Mechanical Engineers, Vol. 49, pp. 321-322 (in Japanese).

Hewitt, G. F., and Hall-Taylor, N. S., 1970. Annular Two-Phase Flow. Pergamon press.

Kataoka, H., Tomiyama, A., Hosokawa, S., Sou, A., and Chaki, M., 2008. Two-phase swirling flow in a gas-liquid separator, Journal of Power and energy systems, Vol. 2, No. 4, pp. 1120-1131.

Kataoka, H., Shinkai, Y., and Tomiyama, A., 2009. Pressure drop in two-phase swirling flow in a steam separator, Journal of Power and Energy Systems, Vol. 3, No. 2, pp. 382-

392.

Katono, K., Ishida, N., Sumikawa, T., and Yasuda, K., 2014. Air-water downscaled experiments and three-dimensional two-phase flow simulations of improved steam separator for boiling water reactor, Nuclear Engineering and Design, Vol. 278, pp. 465-471.

Kitoh, O., 1991. Experimental study of turbulent swirling flow in a straight pipe. Journal of Fluid Mechanics, Vol. 225, pp. 445-479.

Kurimoto, R., Takeuchi, Y., Minagawa, H., and Yasuda, T., 2022. Liquid film thickness of upward air-water annular flow after passing through 90° bend, Experimental Thermal and Fluid Science, Vol. 139, 110735.

Liu, W., Lv, X., and Bai, B., 2020. Axial development of air-water annular flow with swirl in a vertical pipe, International Journal of Multiphase Flow, Vol. 124, 103165.

Nakao, T., Saito, Y., Souma, H., Kawasaki, T., and Aoyama, G., 1998. Droplet behavior analyses in the BWR dryer and separator, Journal of Nuclear Science and Technology, Vol. 35, No. 4, pp. 286-293.

Oliemans, R. V. A., Pots, B. F. M., Trompé, N., 1986. Modeling of annular dispersed two-phase flow in vertical pipes, International Journal of Multiphase Flow, Vol. 12, pp. 711-732.

Takamasa, T., and Hazuku, T., 1998. Measuring a film flowing down a vertical wall using laser focus displacement meters, 1st report Measuring principle and film thickness, Transactions of the Japan Society of Mechanical Engineers Series B, Vol. 64(617), pp. 128-135 (in Japanese).

Wallis, G. B., 1969. One-Dimensional Two-Phase Flow. McGraw-Hill, New York.

Yajnik, K. S., and Subbaiah, M. V., 1973. Experiments on swirling turbulent flows. Part 1.

Similarity in swirling flows. Journal of Fluid Mechanics, Vol. 60, pp. 665-687.

Zhang, Z., Wang, Z., Liu, H., Gao, Y., Li, H., and Sun, B., 2019. Experimental study on entrained droplets in vertical two-phase churn and annular flows, International Journal of Heat and Mass Transfer, Vol. 138, pp. 1346-1358.